Characterization of Hydrophobic Silane Film Deposited on AISI 304 Stainless Steel for Corrosion Protection

E.T. Akinlabi, A.D. Baruwa, O.P. Oladijo, N. Maledi, and J. Chinn

(Submitted August 27, 2018; in revised form July 14, 2019)

This present study was conducted to determine the aptitude of hydrophobic silane coating in corrosion resistance of AISI 304 stainless steel substrate at the nanoscale. Three newly developed hydrophobic silane-based compounds of compositions, namely [tris(trimethylsiloxy)silyethyl]dimethylchlorosilane (alkyl); tridecafloro-1,1,2,2-tetrahydrooctyltrichlorosilane (FOTS); and henicosyl-1,1,2,2-tetrahydrododecyltri-cholrosilane (FDDTS), were used as precursors to coat AISI 304 stainless steel surfaces. Prior to deposition, the substrate surfaces were pretreated with plasma oxide via a multi-step treatment to serve as adhesion. The plasma oxide and the silane precursors were deposited by using a hybrid atomic layer deposition and chemical vapor deposition process. The structural, chemical and electrochemical stabilities were investigated using SEM, AFM, XRD, ATR-FTIR, potentiodynamic polarization and electrochemical impedance spectroscopy (EIS). The results showed that the microstructures and morphology of the coated samples were similar, due to the chlorosilane functionalization. The FTIR indicated complete hydrolysis at the nanoscale while the polarization results showed that nano-coating can hamper the corrosion propagation mechanisms. Furthermore, the EIS results revealed that all the precursors acted as a barrier to AISI 304 dissolution into the electrolyte. The electrochemical effect was observed in the microstructural transformation of the coatings. Although all the precursors were shown to have been effective at few nanoscales, the stability of the FDDTS showed to have superseded that of alkyl and FOTS.

1. Introduction

Stainless steel has been deployed for many applications (where excellent mechanical and high corrosion resistance performance is required). AISI 304 is austenitic, and it contains low carbon and a large amount of chromium. Its surface oxidizes to form a thin chromium oxide layer, which acts as a barrier and prevents corrosion from taking place on the surface of the stainless steel. The oxide film is invisible, durable, superadherent and self-repairing (Ref 1).

Corrosion has been a major concern for the material engineering world. Corrosion occurs in many forms that can be categorized as general corrosion, localized corrosion, pitting corrosion, crevice corrosion, microbial-influenced corrosion (MIC), corrosion fatigue, stress corrosion cracking and galvanic corrosion, among others (Ref 2). All these different forms of corrosion are problems associated with metals. AISI 304 stainless steel has been reported to be susceptible to corrosion on its exposure to harsh environments, such as the acidic environment (Ref 1, 3-6). Seawater has proved to be a corrosive medium for AISI 304 (Ref 7). Corrosion problems related to these aggressive environments have led to numerous investigations that were intended to mitigate the corrosion of AISI 304 SS.

A coating was found to be an effective measure to combat corrosion. The addition of hexavalent chromium Cr^{+6} in coatings has proved to be beneficial and efficient in protecting most metal alloys at extreme temperatures coupled with good wear resistance and corrosion resistance. At the same time, it was found to have its shortcomings, which among others is a carcinogenic effect. Chromium Cr^{6+} in this form is not responsible for the health damage, until it is reduced to Cr^{5+} chemically (Ref 8). It was recommended that the chromium-based coating should be phased out completely before the end of 2007.

Silane is one of the organic coatings that have been developed by researchers to replace the legislated chromium-containing substances (Ref 9). Silane is a thin film that is very durable and reliable (Ref 10, 11). Silane has been used for different applications, such as surface anti-corrosion treatments, additives and adhesives (Ref 12) on a wide range of substrates, such as glass (Ref 13), metals (Ref 11, 14-17), ceramics (Ref 18), ceramic quality improver (Ref 19), antireflective in photovoltaic panel (Ref 20-22), concrete reinforcement (Ref 23), biomedical (Ref 24, 25), wood adhesive (Ref 26) and anti-icing (Ref 27).

E.T. Akinlabi, Department of Mechanical Engineering Science, University of Johannesburg, Johannesburg, South Africa; and Department of Mechanical Engineering, Covenant University, Ota, Nigeria; **A.D. Baruwa**, Department of Mechanical Engineering Science, University of Johannesburg, Johannesburg, South Africa; **O.P. Oladijo**, Department of Mechanical Engineering Science, University of Johannesburg, Johannesburg, South Africa; and Department of Chemical, Material and Metallurgical Engineering, Botswana International University of Science and Technology, Palapye, Botswana; **N. Maledi**, School of Chemical and Metallurgical Engineering, University of the Witwatersrand, Johannesburg, South Africa; and **J. Chinn**, Integrated Surface Technologies, Inc., 1455 Adams Dr., Suite 1125, Menlo Park, CA 94025. Contact e-mail: seyiphilip@gmail.com.

However, silane performance is usually affected by surface energy, absorption, adsorption, wet-out, acid–base interaction and covalent reaction (Ref 12). The carbon–silicon are very nonpolar and stable in the presence of alkyl groups, which are primarily responsible for the low surface energy and the eventual formation of the hydrophobic surface (Ref 28).

Silane is known as a monomeric silicon chemical, and when it has at least one functional group, it is known as organosilane (Ref 29). Organofunctional silane is, therefore, the compound that has two or more reactive groups on its silicon atoms, which are the basis of its characteristics. Organofunctional silane usually has a typical molecular structure of X–CH$_2$CH$_2$CH$_2$Si (OR) 3-nR'n, where $n = 0,1,2$. The reactive groups are hydrolyzable "OR" such as methoxy, ethoxy or acetoxy and organofunctional (a non-hydrolyzable organic moiety), and "X," such as epoxy, amino, methacrylate or sulfide. Silane has alkoxy groups that undergo hydrolysis, as well as condensation to form a bond that is Si–O–Si in nature within the monolayer and the surface, which further forms a highly cross-linked film that is hydrophobic by nature (Ref 30).

$$\text{Metal adhesion}: \ Si-OH + M-OH \rightarrow Si-O-M + H_2O$$

$$\text{Crosslinking}: \ Si-OH + Si-OH \rightarrow Si-O-Si + H_2O$$

The reactive groups led to the invention of a different type of silanes, and they have been used to prevent and/or annihilate corrosion occurrence in most metals. Many of the silanes produced in the past proved not to have good corrosion resistance; bis-[(trimethoxysilylpropyl] amine (bis-amino silane) lacked the ability to protect steel and aluminum from corrosion due to its hydrophilic nature. Adding another compound, such as bis[3-(triethoxysilyl)propyl]tetrasulfide (bis-sulfur silane), did show improvement (Ref 9).

But, in the very recent years, using the bis-[triethoxysilyl-propyl] tetrasulfide silane film showed durability in the protection of the metal surface from corrosion (Ref 31). Calabrese et al. (Ref 32) used three different silanes (dimethyl-dimethoxy-silane, N-propyl-trimethoxy silane and octyltri-ethoxysilane) to improve the thermal adsorption of a heat pump. Also, 3-glycidoxypropyltri-methoxysilane, glyci-doxypropyltri-ethoxy silane, octyltriethoxysilane have served as anti-corrosion coatings on AISI 304 and mild steel (Ref 33, 34). Longhi et al. (Ref 35) worked on various ethoxy silanes to inhibit corrosion on mild steel. It was reported that silane is very beneficial in the area of abrasion resistance, free flow, adhesion, pigment and filler dispersion, overall water and chemical resistance (Ref 29). Many of the silanes used for corrosion resistance were of micrometer thicknesses.

Likewise corrosion resistance, the mechanical properties have been improved by reinforcement of the epoxy thin film using (3-aminopropyl) trimethoxysilane (APTMS) for higher tensile strength and (3-glycidoxypropyl) trimethoxysilane (GPTMS) for more ductility (Ref 36). Also, Wan et al. (Ref 37) used silane-functionalized GO (GPTMS-GO) to achieve the same result. Yang et al. (Ref 38) used N-(2-aminoethyl)-3-aminopropyltrimethoxysilane (YDH792) and obtained a robust shear strength of the fiber and epoxy composite. The higher the porosity, the less the hardness value, the less the tensile and less the yield strengths of the material (Ref 39, 40). However, the mechanical interlock factor is responsible for the adhesion of the coating to the surface of the substrate (Ref 41). From the literature reviewed, it is very clear that no organic coating

material is special for all applications. Therefore, the researchers have never stopped to develop the organic materials that would best suit the intended purposes.

However, chlorosilane has not really gained the attention of the researchers in the area of organic surface coatings. Chlorosilanes include the alkyl chlorosilanes, the aryl chlorosilanes and the trichlorosilane. Moreover, trichlorosilane (HSiCl$_3$) has been found to be high-purity silicon, which has found its application largely in the photovoltaic field and its adaptability in electronics until recently, when it has been adopted for metallurgical purposes (Ref 42). Organosilanes, such as chlorosilanes, have been used to a large extent as water-repellants (Ref 43).

It has been found from the literature that a few coatings have been done at 100 nm, while others have been done at greater thicknesses.

The aim of this study is to characterize and investigate the effect of trichlorosilane coatings on the AISI 304 SS via different methods, in order to determine the corrosion behavior of the bare and coated samples at the coating thickness of 20 nm, and finally to establish the best among the three silane compounds that are presented.

2. Experimental

2.1 Material

A commercially available 3-mm-thick stainless steel AISI 304 sourced at Metal Centre, South Africa, was used as the substrate with percentage composition of carbon (0.023), sulfur (0.003), phosphorous (0.028), manganese (1.17), silicon (0.35), chromium (18.1), nickel (8.0), nitrogen (0.07) and balance iron. The bare samples were coated with three different types of silane films, namely tri(Trimethylsiloxy)silyethyl] dimethylchlorosilane (alkyl), tridecafloro-1,1,2,2-tetrahy-drooctyltrichlorosilane (FOTS) and henicosyl-1,1,2,2-tetrahy-drododecyltricholrosilane (FDDTS). These silane films were formulated, prepared and deposited by the Integrated Surface Technologies Inc., San Francisco, USA.

2.2 Preparation of the Coatings

The coatings were deposited on 100×100 mm^2 size 304 stainless steel plates by using a double-layer hybrid atomic layer deposition (ALD) and chemical vapor deposition (CVD) RPX-540 coating equipment manufactured by Integrated Surface Technologies (IST). Before deposition of the hydrophobic compounds, the surfaces of the bare samples were ground up to 800 microns without polish afterward in order to attain strong adherence between coating and substrate. The ground surfaces were cleaned with acetone, followed by ethanol, and then finally dried under a nitrogen stream, and the samples were carefully wrapped and kept in the desiccator to avoid contamination and oxidation.

The surface treatment was a three-step process: from oxygen plasma; followed by water plasma; and lastly, the silanization of the surface. The oxygen plasma treatment was utilized to reform a surface dioxide layer. The water plasma treatment is known to leave the surface hydroxyl group ($^-$OH) terminated. Both the water and the oxygen plasma treatment resulted in clean, flat surfaces free from organic and inorganic contaminants. Silica film was used as an additional base adhesion layer

on samples produced by using deionized water and tetra-chlorosilane. The precursors were heated to the temperature of 150 °C to avoid condensation of the vapor while the temperature of the chamber and the substrate was maintained at 120 °C to prevent coagulation of the deposited films. The resulting silica layer, plasma oxide and silane composite thickness was approximately 20 nm, as measured by the ellipsometry on a reference Si wafer. The silica layers were deposited via a similar procedure, when the chamber pressure was reduced to less than 4 Pa.

2.3 Microstructure and Surface Morphology

The surface morphology and microstructure of the coatings were characterized by a Tescan scanning electron microscope (SEM) (Vega 8) via nanospace software. The imaging was conducted using a secondary electron (SE) and backscattered electron (BSE) for corrosion propagation investigation at 20 kV while maintaining a safe working distance.

The investigation of the surface roughness and the amplitude was performed by using the atomic force microscope (Veeco Di3100 AFM nanoscope). Four different scans were made on each sample, and the averages of the four spectra are reported. The scan data were obtained at tapping modes with a spring constant of $2.8 \ Nm^{-1}$, a resonance frequency of 75 kHz, a scan rate at 2 Hz, a drive amplitude of 840 mV and a scan size at 1 μm × 1 μm.

2.4 X-ray Diffraction Analysis

Phase crystalline structures and crystallite size of the silanes (alkyl, FDDTS and FOTS) and the base material were characterized by using a PANalytical x-ray diffractometer. The radiation source was CuKα, and the scanning parameters were set as the wavelength (λ) equivalent to 1.5418 Å, at 40 kV and 45 mA. The scan range was 5°–90° at 0.0001° steps with 3°/min speed. A sample size of $10 \times 10 \ mm^2$ was prepared for the experiments. The scan was K-beta filtered, and the crystallite size was calculated by using full width at half maximum (FWHM) level for every specific XRD peak, using the Debye-Scherrer formula by the equation:

$$D = \frac{K\lambda}{\beta \cos \theta} \quad \text{(Eq 1)}$$

where β is the broadening of the line at full width at half maximum intensity (FWHM); θ is the Bragg's angle; λ is the x-ray source wavelength; K is the dimensionless shape factor (1); and D is the diameter of the grain size.

2.5 ATR-FTIR

The chemical stability of the coating was investigated by using the PerkinElmer 100 spectrometer attenuated total reflectance Fourier infrared (ATR-FTIR). The spectrometer used a liquid N_2-cooled HgCdTe detector sensitive to the infrared region from 650 to 4000 cm^{-1}. All the spectra were recorded at 2 cm^{-1} resolution. The scans were repeated twice to ensure repeatability.

2.6 Electrochemical Test

The potentiodynamic polarization and electrochemical impedance spectroscopy (EIS) were performed by using the Iviums Technologies' Vertex One potentiostat equipped with IviumSoft version 2.5XX software for the data processing and by strictly following the ASTM G3-89 (Ref 44). The open circuit potential was measured in natural seawater of pH ranging between 8.1 and 8.2, using an Ag/AgCl electrode as a reference, coated and bare samples as the working electrode and the platinum wire of 0.5 mm diameter as the counter electrode. The measurements were conducted over the frequency range of 10-10 mHz (peak to zero) and at a perturbation amplitude of 1 mV sinusoidal voltage. The scan rate was set at 0.5 mVs^{-1}, and the working electrode was immersed in the electrolyte for a period of 1 h to obtain a stable open circuit potential of the materials. The investigation was conducted three times on every sample, to ensure the repeatability of the result.

3. Results and Discussion

3.1 Scanning Electron Microscope (SEM)

The SEM analysis depicted in Fig. 1 shows that all the coated samples have a similar, discrete and mixed microstructure that is characterized as varying grain sizes. The similarities in the observed microstructure may be attributed to the same functional group (chlorosilane) of the coating material. The coated samples were uniform and without any micro-cracks, thus showing homogeneity and chemical stability of the organic coating material and the deposition process. Also, the topography of the coating microstructure shows a sea-island structure (Fig. 1). Similar observations were reported by Boutamine et al. (Ref 45).

3.2 Atomic Force Microscope (AFM)

The atomic force microscope (AFM) was further used at a tapping mode to characterize the topography of the AISI 304 sample and the coated films, with acquisition taken at 1 μm². Details of the grain sizes and roughness of the investigated samples are presented in Fig. 2 and Table 1. From the mean and average roughness of the data captured and the imaging, it is observed that the organic coatings were not relatively smooth when compared with the base material, as shown in Table 1. The coating also appeared to be ultra-thin in thickness, and it couldn't fully submerge the asperities present on the surface of the base material—even though the surface of the base material was fully covered. The roughness of the coating surface is necessary to retain its hydrophobicity.

However, there were no particulate accumulations in the process of the coating, as in the case of dichlorodimethylsilane (Ref 46). It is also evident from the investigation that there were no cracks that could have caused film dilapidation through diffusion.

3.3 X-ray Diffraction (XRD)

From the x-ray diffraction results (Fig. 3), it is evidence that there are five major peaks that are associated with the bare and the three coated samples under investigation at phases 011, 012, 111, 220 and 222. The peaks show no difference in the diffraction pattern with respect to the base material. The peaks were found around $2\theta = 43.5°$, $44.4°$, $50.7°$, $74.6°$ and $82.3°$. It is evident that iron (Fe) and silicon (Si) are the dominant elements from all the peaks and in the phases generated from
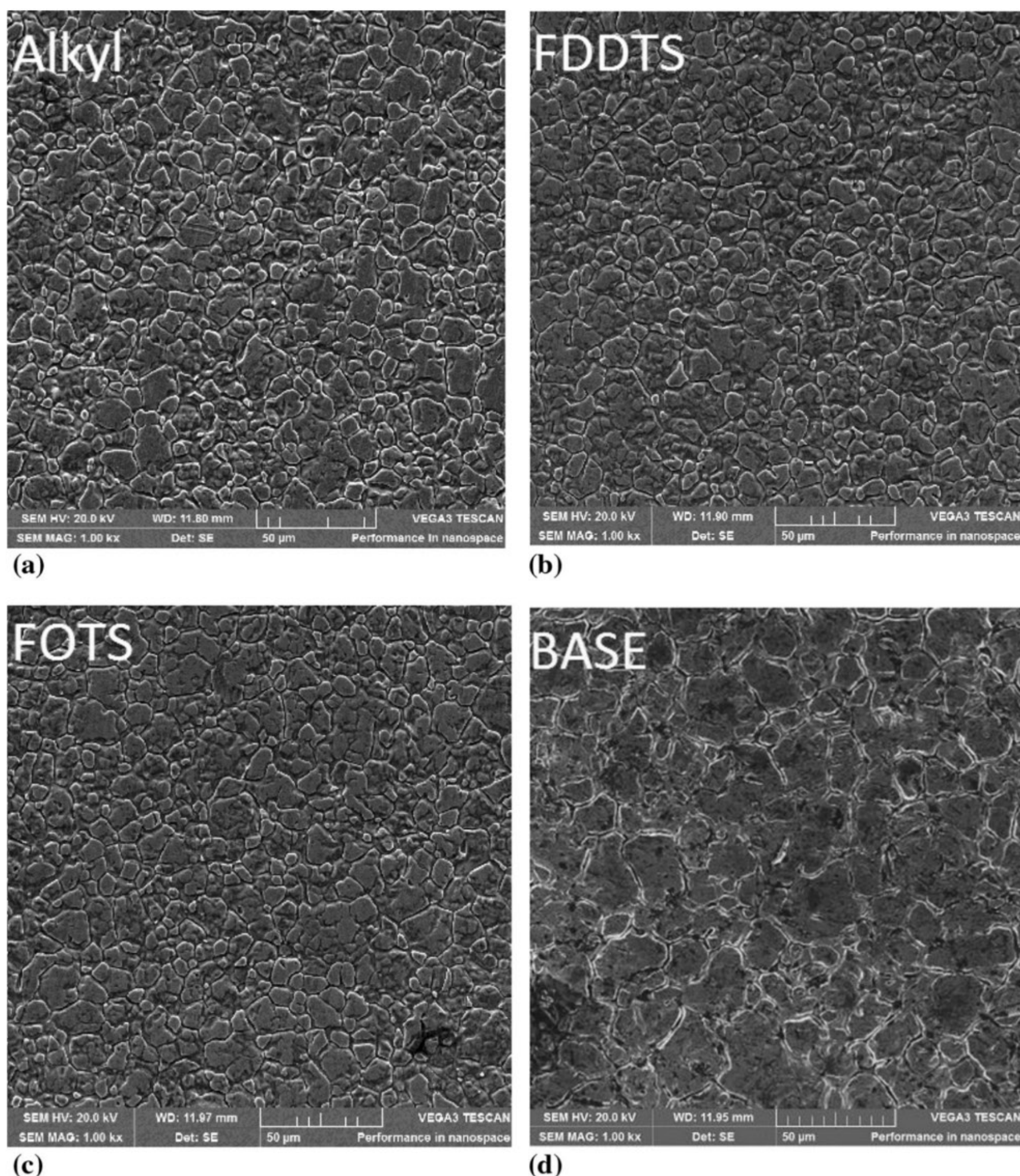
Fig. 1 SEM images of coated samples and the base: (a) alkyl; (b) FDDTS; (c) FOTS) and (d) base, before the corrosion test

the diffraction. However, it is only Fe that was diffracted on the bare AISI 304, while all the other coating materials showed silicon, together with a combination of Fe and carbon (C).

There are mixed phases in all the peaks except 2-theta at approximately 50.7°. There is no evidence of any peak shift from the base material, even though there are instances of mixed patterns from the coated samples. Lack of shifts in all the silane compounds means that the organofunctional copolymerization does not in any way affect the peak diffraction (Ref 47). There was an expectation of complete exfoliation of Fe from the surface of the coated samples, but the dominance of iron phase on the coated samples could be as a result of the thickness of the thin film at 20 nm. The crystallite sizes calculated from Scherer's formula are between 24 and 105 nm for the base material, 17 and 89 nm for the alkyl, 17 and 161 nm for the FDDTS and 19 and 84 nm for the FOTS, which are all within the range predicted by the AFM.

3.4 ATR-FTIR

The stability of the films (chemically) was further probed by using the attenuated total reflectance Fourier transform infrared

(ATR-FTIR). In Fig. 4, the spectra of the silane films are presented, and the associated bands and interpretations are presented in Table 2. The silane films of alkyl, FDDTS and FOTS have the absorbance of stretched silane compounds at 2199 cm^{-1}. This is an indication of the presence of a functional group in the films' compound matrixes, and the Si-H functional group absorbance is independent of the chemical composition of the compounds under investigation. Multiple ranges of strong Si-O-Si bending and stretching at 1051 cm^{-1} for alkyl and FDDTS, while stretching at 1049 cm^{-1} wavelengths, are observed in all the silane compounds. A C–H bending is observed at 1333 cm^{-1} for FOTS while Si-O-Si stretching is observed at 1344 and 1346 cm^{-1}, respectively, for alkyl and FDDTS. An isosbestic-like point can be observed for C=CH axial stretching at 1633 cm^{-1} when the spectra are superimposed on one another. C–H bending bands are observed at 696, 693 and 694 cm^{-1} for alkyl, FDDTS and FOTS, respectively. C–H (CH_2=CH_3) symmetric and asymmetric stretching is absorbed at 2911 cm^{-1} as a result of hybridization which in turn enhances bonding property of a compound and could further influence its molecular geometry.
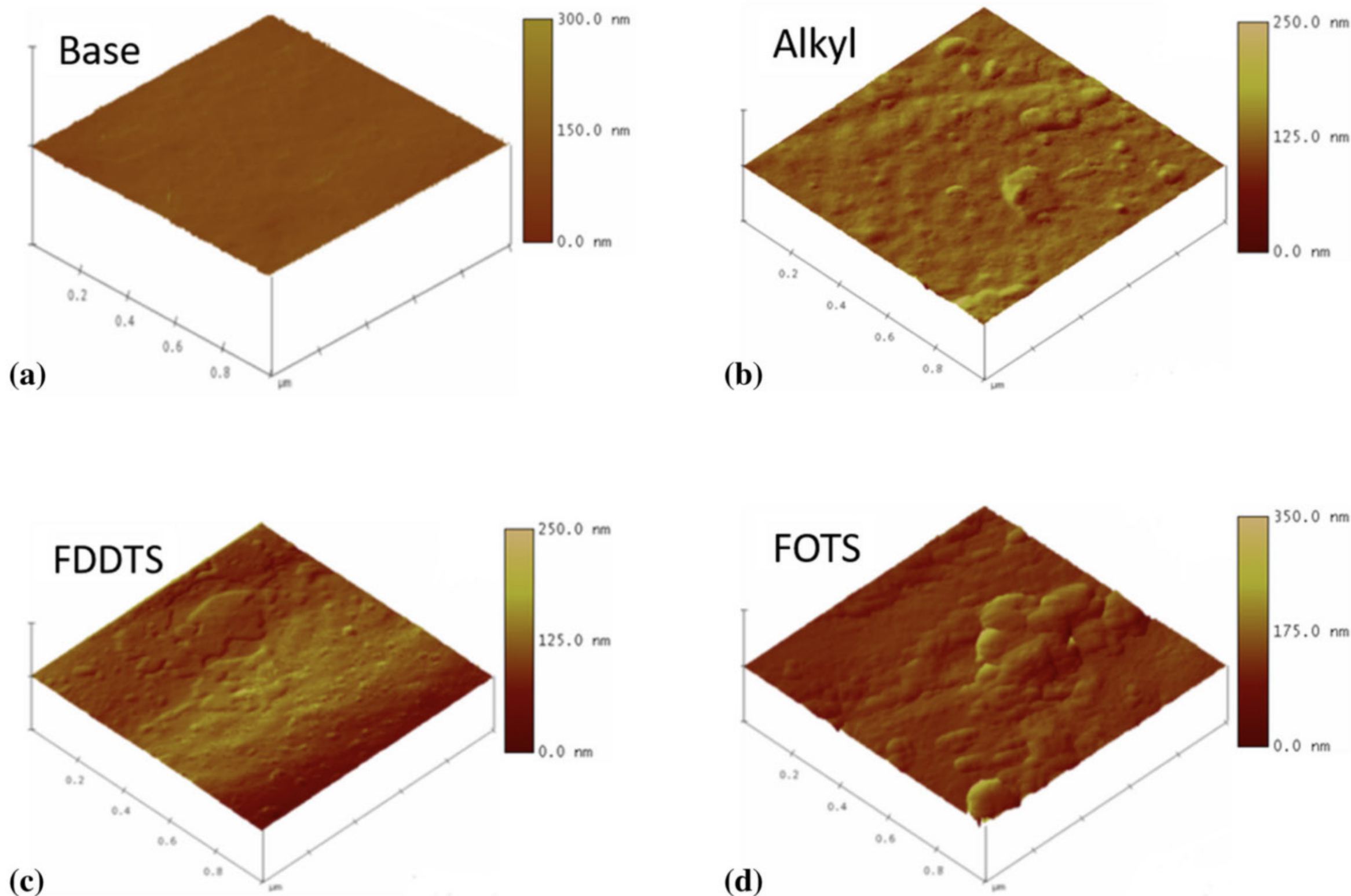
Fig. 2 AFM images of different coatings for: (a) bare, (b) alkyl, (c) FDDTS and (d) FOTS samples, respectively

Table 1   AFM summary of the data captured from the scans

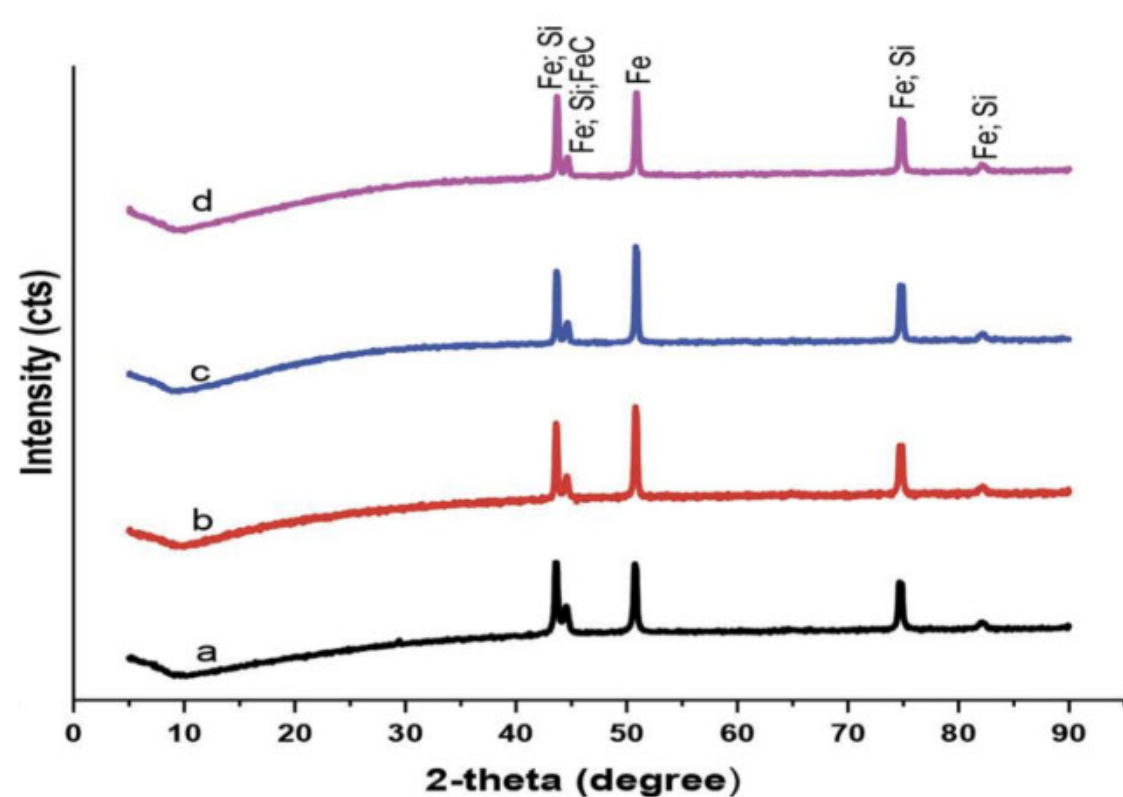| Sample	Rms, nm	Ra, nm	Surface area, μm^2	Grain size range, nm
Bare	7.39 ± 3.1	6.14 ± 0.8	1.11 ± 0.3	13.71–1233.51
Alkyl	11.03 ± 2.3	8.04 ± 1.1	1.13 ± 0.2	19.53–1438.61
FDDTS	11.34 ± 2.9	8.31 ± 2.8	1.14 ± 0.3	19.81–1512.32
FOTS	5.11 ± 7.6	7.11 ± 9.5	1.05 ± 0.1	19.56–1060.12

Fig. 3 XRD spectra of coated and uncoated samples' surfaces of (a) base material, (b) alkyl, (c) FDDTS and (d) FOTS

The peak at 1049 cm^{-1} or near agrees with the work of Aydınoğlu and Yoruç (Ref 48). The frequencies of appearance of Si–O–Si in the spectra of all the silane films depict complete hydrolysis of the thin films during curing. Additionally, it means that an effective protecting layer was exerted on the AISI 304 substrate. However, at 3267 cm^{-1} in the spectrum of FOTS, broadband of Si–OH stretching was observed, which is characterized as axial deformation, and it depicts a hydrophilic effect. This could increase the hydrophilicity of the surface and cause a quick breakdown of the silane film by –OH group, which supports the water uptake and could assist in the hydrolyzation during exposure to the electrolyte.

3.5 Corrosion Test

3.5.1 Potentiodynamic Polarization. The electrochemical tests were performed in seawater solution to study the rate at which corrosion occurs and the susceptibility of the base material and the coated samples to the corrosive medium.

Table 3 shows the values of the corrosion potential (E_{corr}), the current density (I_{corr}), the corrosion resistance (R_p), anodic Tafel reaction (b_a), cathodic Tafel reaction (b_c) and the corrosion rate. These factors could be described as

$$b_{a/c} = 2.303 * B \quad \text{(Eq 2)}$$

where

$$B = \frac{b_a \cdot b_c}{2.303(b_a + b_c)} \quad \text{(Eq 3)}$$

and it is equivalent to Stern–Geary constant V, whereas

$$I_{corr} = \frac{B}{R_p} \quad \text{(Eq 4)}$$

The graphical representations of the data generated are shown in Fig. 5.

From the results presented in Fig. 5, it is evident that there were shifts in both the anodic and the cathodic readings of the coated samples. The E_{corr} of the alkyl and FDDTS shifted in a positive direction and formed anodic polarization, while the FOTS became more negative and cathodic. This shows a different approach to corrosion inhibition, a case similar to that of Nasrin et al. (Ref 49). FOTS also inhibits corrosion through cathodic protection, which means that the electrode potential of FOTS is more active than that of the other coatings. However, the shift toward the positive means that the presence of alkyl and FDDTS coatings on the surface stalled the anodic dissolution and decelerated the oxygen absorption to the substrate's surface.

The shift further indicates that the current density exchange for the evolution of hydrogen is lower than that of alkyl and FDDTS, while at the same time, the current exchange for the dissolution of FOTS in the electrolyte is higher than that of the two other coatings. The I_{corr} decreased significantly for the alkyl and FDDTS coatings, while there was a slight decrease in the current density of FOTS. Also, the less I_{corr} value of FOTS means that it cannot alter the mechanism at which the corrosion occurs, but it can improve the barrier to the rate at which corrosion occurs, while alkyl and FDDTS can change the mechanism by their high corrosion potentials. Protecting the surface of steel from corrosion would require the film to depend only on a barrier mechanism (Ref 50). This is evident in the rate at which corrosion occurs in all the coated samples. Table 3 shows the corrosion rate per year of every sample; all the coated samples have a lower corrosion rate, but alkyl and FDDTS happened to reduce significantly. The efficiency ($P\%$) of the coatings to initiate corrosion protection was also measured from the current density (I_{corr}) by using the relationship between the current densities of the base material and the coated samples (Ref 51) in Eq 5:

$$P\% = \left(\frac{I_{corr}^b - I_{corr}^c}{I_{corr}^b} \right) \times 100\% \quad \text{(Eq 5)}$$
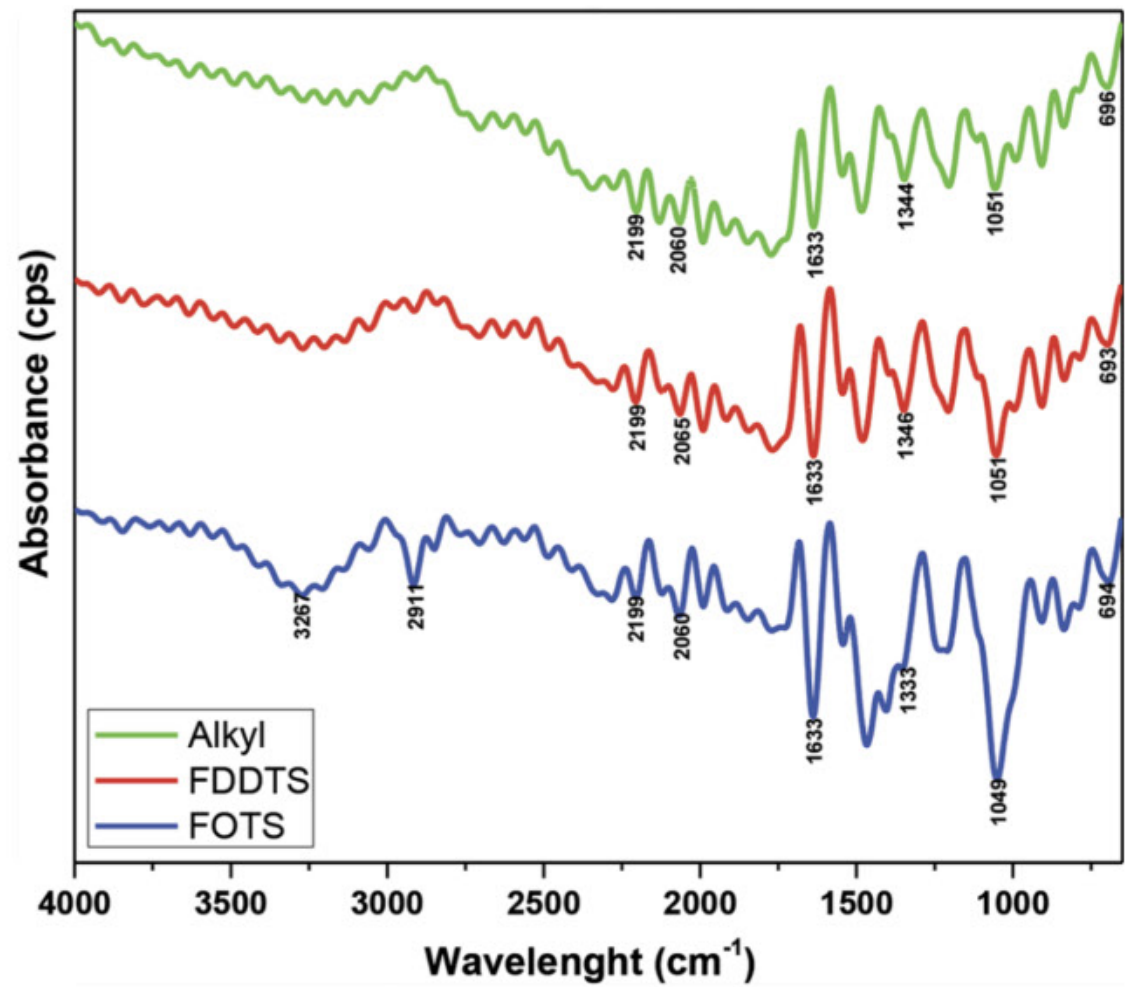

Fig. 4 ATR-FTIR spectra of the organic hydrophobic-coated samples; green (alkyl); red (FDDTS); and blue (FOTS) prepared by using surface pretreatment of plasma oxide (Color figure online)

Table 2 ATR-FTIR incidence on the coated samples and the peak assignment

Peak position, cm^{-1}	Peak assignment (band)
600–700	C–H bending
1000–1200	Si–O–Si stretching
1300–1400	C–H bending, Si–O–Si stretching
1600–1670	C=CH axial stretching
2000–2400	C=C=O stretching
2100–2360	Si–H stretching
2900–3000	C–H (CH$_2$=CH$_3$) symmetric and asymmetric stretching
3200–4000	Si–OH broad/sharp stretching

Table 3 Summary of potentiodynamic polarization extrapolations

	Base	Alkyl	FDDTS	FOTS
E_{corr}, V	− 0.2661 ± 00	− 0.2615 ± 0.001	− 0.2294 ± 0.004	− 0.3444 ± 0.001
I_{corr}, A cm^{-2}	1.52E − 05 ± 00	7.37E − 06 ± 0.090	5.38E − 06 ± 0.056	1.69E − 5 ± 0.103
R_p, Ω.cm^2	2398 ± 00	2929 ± 057	2857 ± 038	2228 ± 41
b_a, v/dec.	0.106 ± 00	0.077 ± 0.003	0.040 ± 0.011	0.086 ± 0.006
b_c, v/dec.	0.404 ± 00	0.139 ± 0.013	0.291 ± 0.007	0.152 ± 0.003
C_{rate}, mm/yr	0.1632 ± 00	0.07889 ± 0.00003	0.05756 ± 0.00009	0.1144 ± 0.00001
Efficiency, %	…	51.51	64.61	11.18

where I_{corr}^b and I_{corr}^c are the current densities of the base material and the coated surfaces, respectively.

The efficiency is an indication that the thin film was able to hamper the diffusion of electrolyte to the surface of the substrate even at 20 nm thickness.

3.5.2 Electrochemical Impedance Spectroscopy (EIS).

Further investigation was conducted using EIS to determine the competence and the capability of the anti-corrosive property of the organic coatings as regards the thickness on bare SS304 in natural seawater. The OCP values derived were used to generate the results presented in Table 4, and the fittings were made through the electrical circuits in Fig. 6 (Fig. 6a for uncoated surface and Fig. 6b for the coated surface).

The Bode diagrams (Fig. 7a) show two time constants (high and low frequencies) for all the coated samples, while the uncoated sample has only one time constant. The low-frequency time constant implies that the film delays the corrosion process by sealing the possible distributed pores on the samples. From the graph, it is noted that at high frequencies, all the coated samples have low phase angles and high phase angles at low frequencies. Meanwhile, only FDDTS has a high phase angle that matches up with that of the base material, while all the silanes have more than the base material at high frequencies.

However, the high phase angle of the substrate could be due to high chromium in the chemical matrix of the material, which also serves as an anti-corrosion agent. This means that alkyl and FOTS have a low barrier response to the electrolyte at low frequencies, but their susceptibility to corrosion outlasts that of the base material as the frequency increases. The Nyquist plot was explored to determine the resistance capability of the coatings on the substrate. Figure 7(c) shows that the capacity loops of bare, alkyl, FDDTS and FOTS are different and depressed, which is an indication of the charge transfer resistance of the corrosion process on the coatings and the base material. The capacity loops of the coated samples are not perfect semicircles which could be attributed to the frequency distribution of inhomogeneity and/or the roughness of the working electrodes (Ref 25). This is the basic reason why the "power law-dependent" interfacial capacity which justifies the coating and the oxide has been expressed as a constant phase element (CPE) for roughness and the imperfections on the substrate and the coated surfaces. The equation is given as (Ref 52):

$$Z_{CPE} = \frac{1}{Y_o(j\varpi)^n} \qquad \text{(Eq 6)}$$

where j is the imaginary unit; Y_o is the CPE constant; ϖ is the angular frequency; and n is the CPE exponent (that represents the deviation from the ideal behavior and it lies between 0 and 1).

From Fig. 7(c), the AISI 304 spanned at almost an angle of 45°, which could be an indication of diffusion process occurring at a slower rate than the metal charge transfer reaction on the metal oxide layer (Ref 53). It could also mean a possibly quick susceptibility or porosity of the protecting oxide
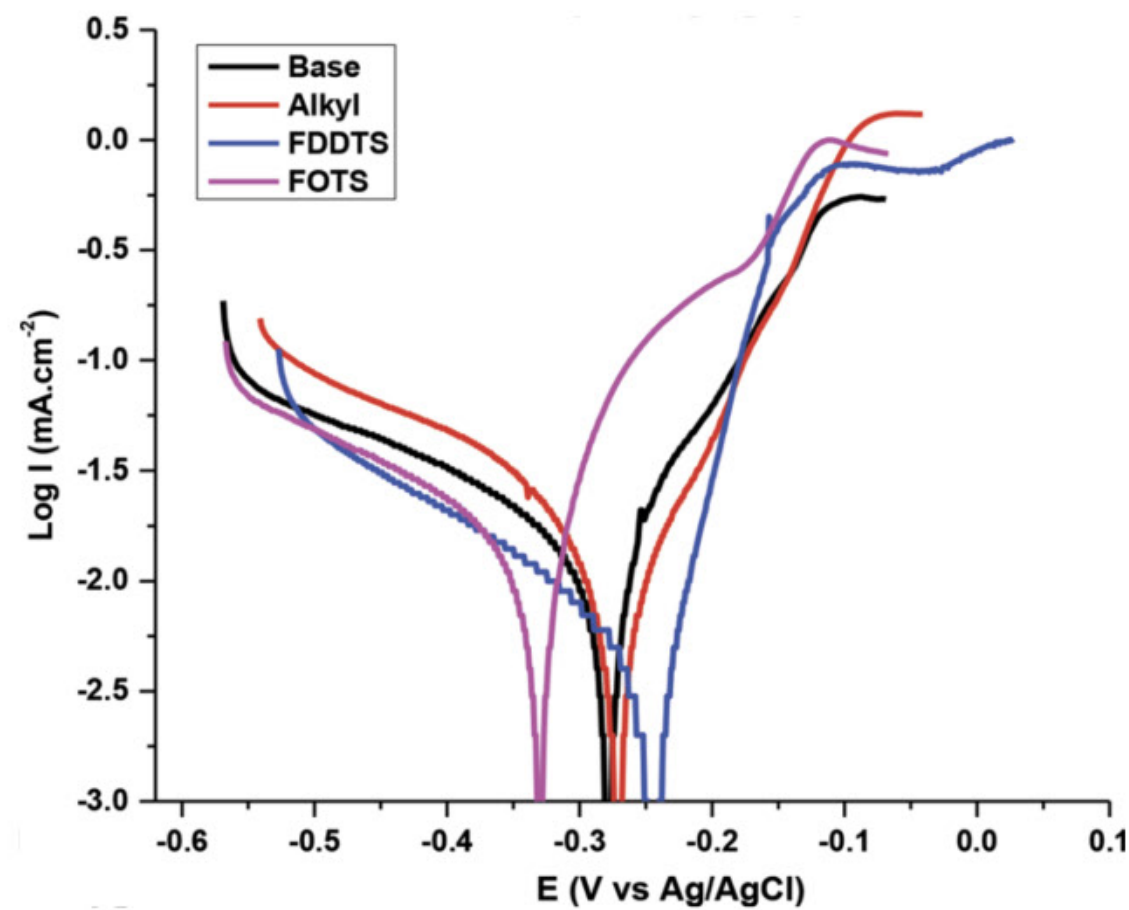

Fig. 5 Summary of the potentiodynamic polarization test results (Tafel extrapolation) of the coated samples and bare AISI 304 stainless steel
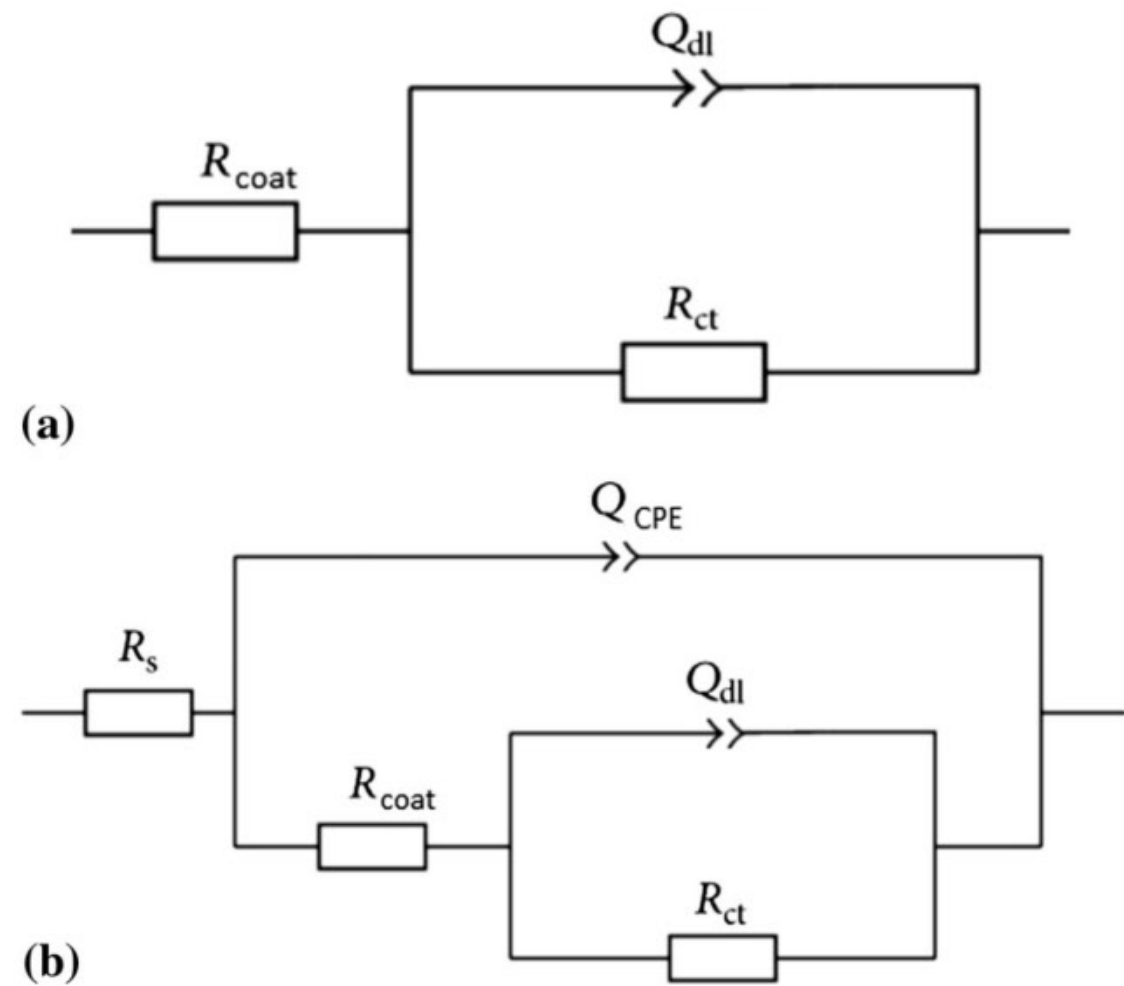

Fig. 6 Electrical circuits used for the fittings of (a) base material, and (b) coated samples

Table 4 EIS fittings for the bare and coated samples

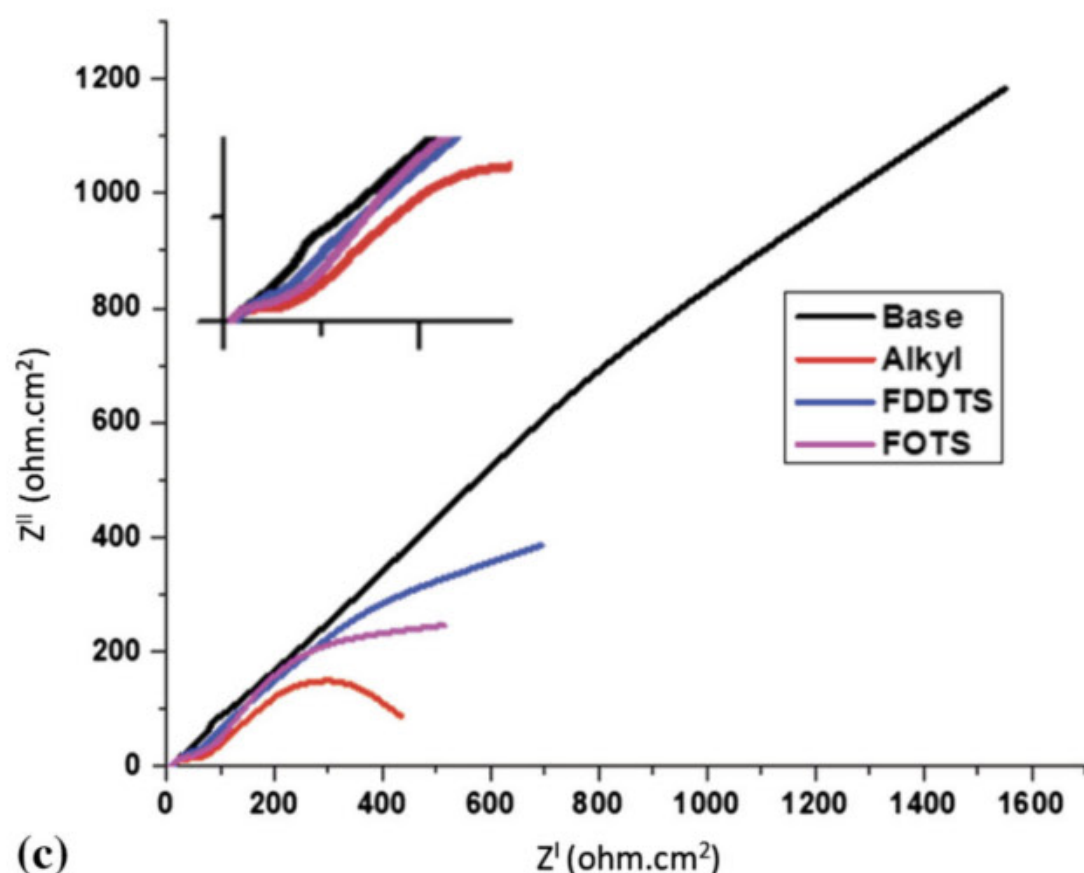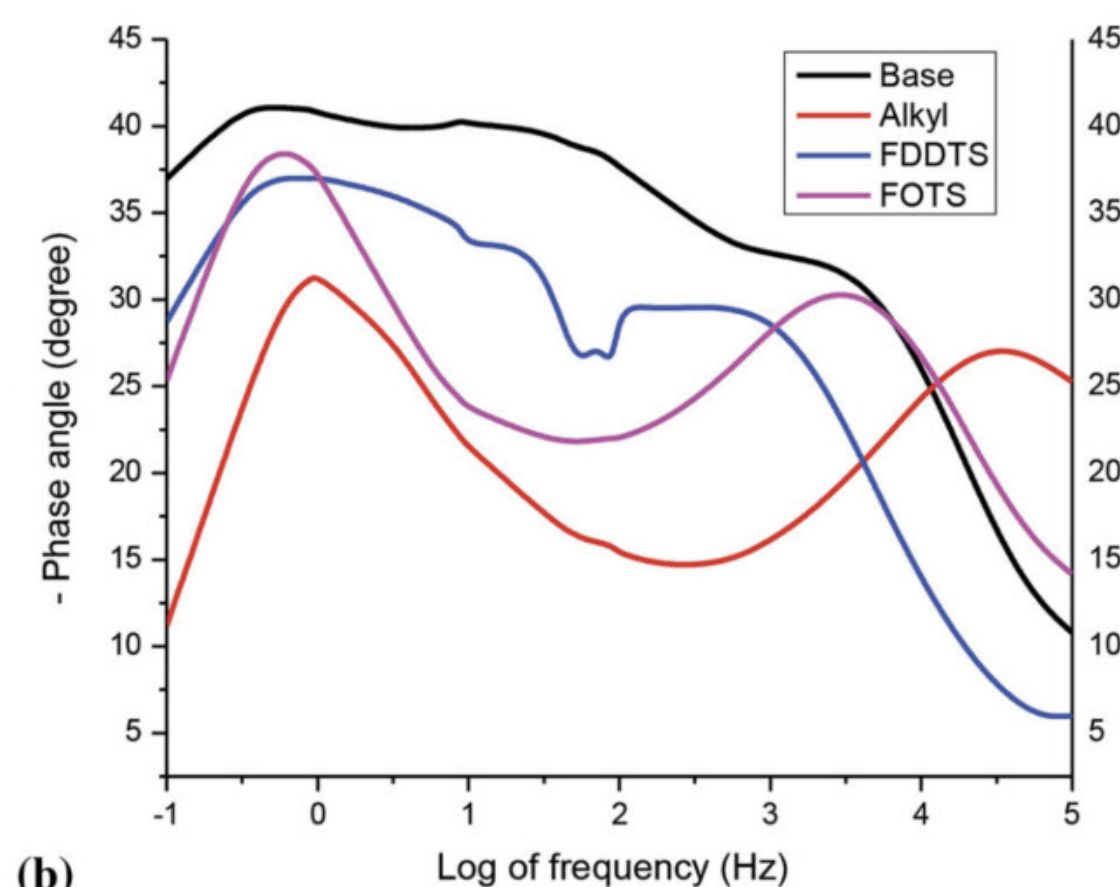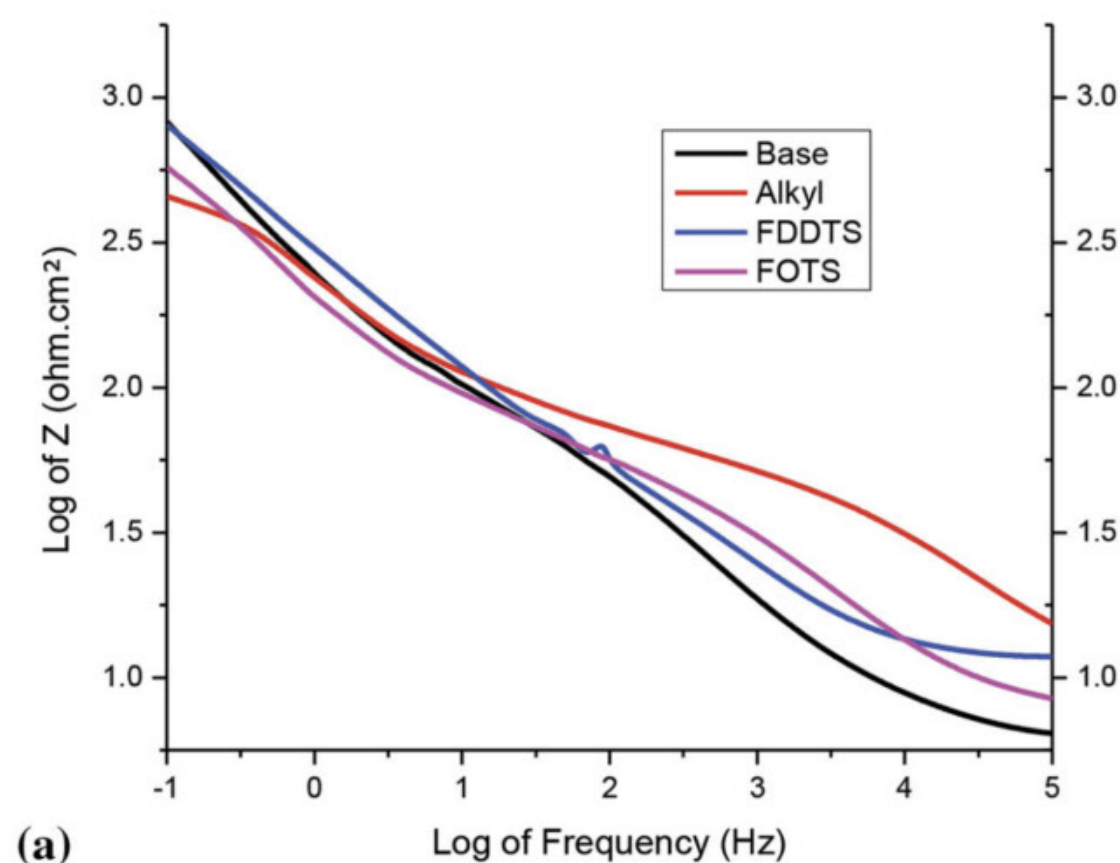| Material	R_s, $\Omega.cm^2$	R_{ct}, $\Omega.cm^2$	R_{coat}, $\Omega.cm^2$	C_{dl}, $\mu F\ cm^{-2}$	CPE Y_0, $n\mu F\ cm^{-2}$	n
Base	109 ± 0.0	1550 ± 0.0			306.4	0.81
Alkyl	036 ± 0.5	0433 ± 1.1	074 ± 0.4	0938 ± 1.3	020 ± 1.3	0.90
FDDTS	034 ± 0.7	0693 ± 0.8	267 ± 0.6	1418 ± 0.8	170 ± 0.8	0.85
FOTS	028 ± 0.4	0513 ± 0.7	110 ± 0.9	1440 ± 0.7	088 ± 1.4	0.76

Fig. 7 EIS plot; (a) Bode plot, (b) Phase diagram, (c) The Nyquist plot, at room temperature in natural seawater solution

layer on the material (Ref 53, 54), while the coated samples have widespread semicircles which depict the protective capability of the film or coating. As the diameter of the capacitance loop increases, the more the corrosion rate decreases. This is in accordance with the electrochemical theory which states that the corrosion rate and the charge

transfer resistance are proportional. The bigger the diameter of the capacitance loop, the harder is the electron transfer and the diffusion at the solution–metal interface. Hence, it is thought that the corrosion prevention of the coated samples did not happen because of anodic or cathodic charge transfer, but via the barrier enabled by the coating film thickness.

Among the coated samples, FDDTS reveals the greatest impedance, while FOTS shows a high value for the constant phase element (CPE). Low frequency and low imaginary impedance show the ability of the film to reduce the rate of diffusion of corrosive electrolyte onto the surface of the stainless steel.

On the other hand, Fig. 8 shows the micrograph of the bare AISI 304 and the coated samples after corrosion. The figure shows that the protective oxide film of the base material was attacked and became dilapidated, while the FDDTS, alkyl and the FOTS films showed dark spots, a revelation of resistance to aggressive film breakdown, which is also an indication of pitting corrosion initiation. However, FDDTS shows better resistance against corrosion, as it indicates the least localized pitting spots. Furthermore, it can be noted from the images that the grains of the films underwent transformations. The discrete grains appeared to have fallen and ruptured. The grains looked entangled, meshed and muddled up after corrosion processes.

4. Conclusions

A stainless steel substrate was treated at different stages, and it was coated with three different silanes (alkyl, FDDTS and FOTS). These samples were subjected to different characterizations to establish their viability, and the results can be summarized as follows:

- SEM suggested that the AISI 304 was susceptible to seawater and the effect can be minimized or abolished by applying an organic coating to the surface. The organic coating of 20 nm can reduce the rate of corrosion by a barrier and/or through repulsion of water, while a thicker organic coating could perform better.
- Although the AFM results indicated that the FOTS appeared to be the best coating material, all the other coating materials also exhibited good performances over the base material.
- The FTIR result indicated that the coating was efficient and functional by adsorbing the Si–O–Si siloxane network—an indication of complete hydrolysis during the curing process.
- The asperities present in the coated samples because of scratches were not enough to initiate or accelerate the rate of corrosion. This suggests that less thin coatings of these silane compounds could still hamper or inhibit the rate of corrosion.
- From the corrosion perspective, it has shown that organic coatings can effectively prolong the service life of metal (SS 304), even at a coating thickness of about 20 nm. The possible pores and defects present in the base samples were blocked by silane coatings. This level of thickness could be accommodated and useful where coatings are almost prohibited due to safety precautions.
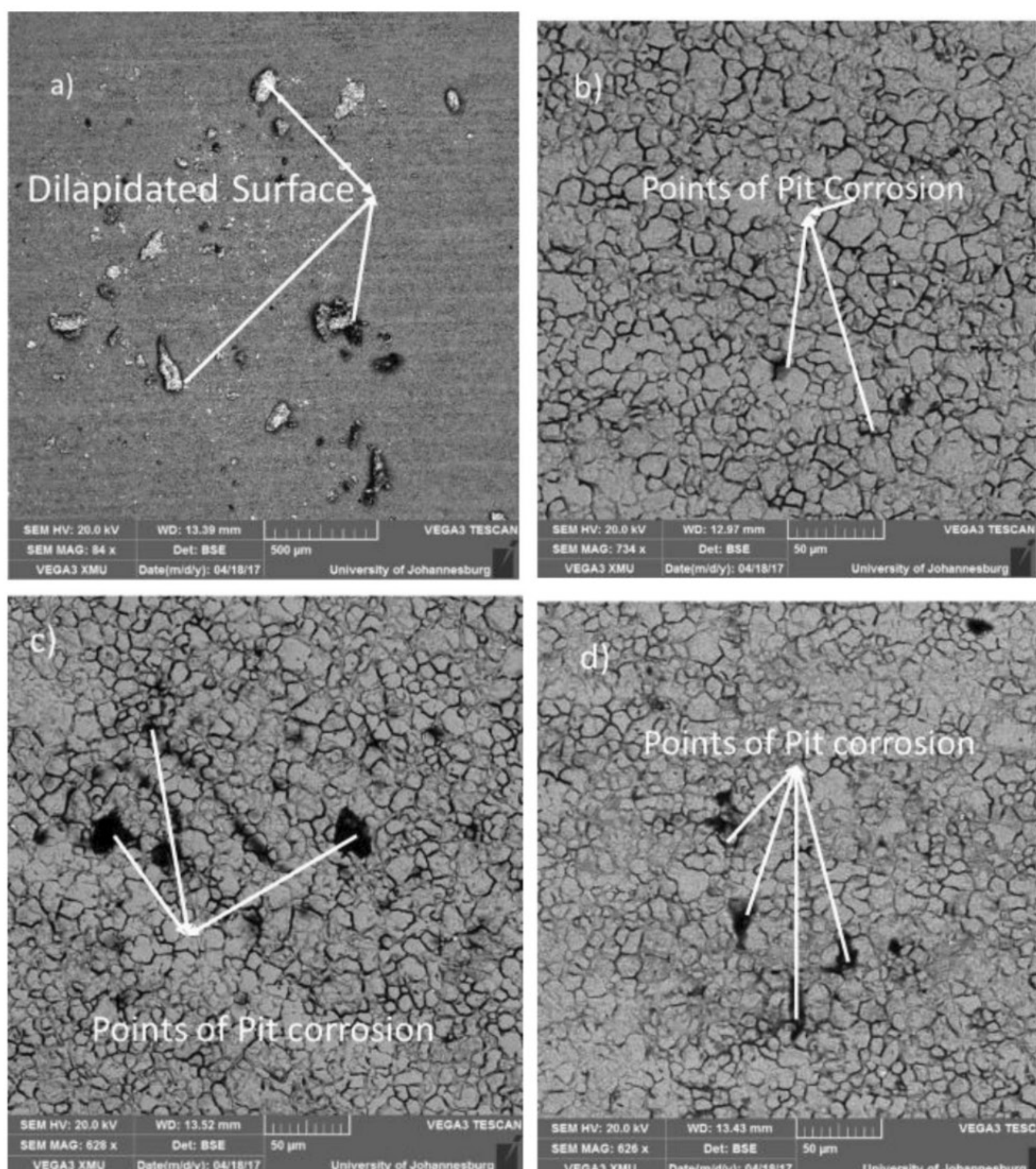- From all the characterizations, FDDTS proves to be the

Fig. 8 SEM images of: (a) bare AISI 304, (b) FDDTS, (c) alkyl and (d) FOTS after samples were subjected to the electrochemical test

best organic coating material due to its hydrophobic composition of $CH_3–(CH_2)_7$ group over alkyl and FOTS of $CH_3–(CH_2)_9$ and $(CH_2)_2$ groups, respectively.

References

1. R.T. Loto, Pitting Corrosion Evaluation of Austenitic Stainless Steel Type 304 in Acid Chloride Media, *J. Mater. Environ. Sci.*, 2013, **4**(4), p 448–459
2. Special Metals Corporation, *High-Performance Alloys for Resistance to Aqueous Corrosion*, Special Metals Corporation, 2000, p. 61. http://www.specialmetals.com/
3. R.S. Oguike, Corrosion Studies on Stainless Steel (FE6956) in Hydrochloric Acid Solution, *Adv. Mater. Phys. Chem.*, 2014, **04**(08), p 153–163
4. I. Iliyasu, D.S. Yawas, and S.Y. Aku, Corrosion Behavior of Austenitic Stainless Steel in Sulphuric Acid at Various Concentrations, *Adv. Appl. Sci. Res.*, 2012, **3**(6), p 3909–3915
5. A.S. Afolabi, J.H. Potgieter, A.S. Abdulkareem, and N. Fungura, Effect of Tempering Temperature and Time on the Corrosion Behaviour of 304 and 316 Austenitic Stainless Steels in Oxalic Acid, *World Acad. Sci. Eng. Technol.*, 2011, **79**(7), p 528–532
6. W.Y. Lai, W.Z. Zhao, Z.F. Yin, and J. Zhang, Electrochemical and XPS Studies on Corrosion Behaviours of AISI, 304 and AISI, 316 Stainless Steels under Plastic Deformation in Sulphuric Acid Solution, *Surf. Interface Anal.*, 2012, **44**(5), p 505–512
7. Z. Hai-lin, Y. Shu-jun, and Z. Peng, Evaluation of Fatigue and Corrosion, Analysis and Comparison with Hardness for Stainless Steel—304, *J. Eng.*, 2017, **1**(1), p 22–32
8. X. Shi and N.S. Dalal, Generation of Hydroxyl Radical by Chromate in Biologically Relevant Systems: Role of Cr(V) Complexes versus Tetraperoxochromate(V), *Environ. Health Perspect.*, 1994, **102**(SUPPL. 3), p 231–236
9. D.W. Schaefer, G. Pan, and W. Van Ooji, Anticorrosion Coatings: Can They Be Made without Chromium?, *Los Alamos Sci.*, 2006, **30**, p 172–177
10. A.N. Rider, Factors Influencing the Durability of Epoxy Adhesion to Silane Pretreated Aluminium, *Int. J. Adhes. Adhes.*, 2006, **26**(1–2), p 67–78
11. J. Yu, S. Liu, F. Li, and T. Wang, Na2SiO3/Al2O3 Composite Coatings on 304 Stainless Steels for Enhanced High Temperature Oxidation Inhibition and Chloride-Induced Corrosion Resistance, *Surf. Coat. Technol.*, 2017, **309**, p 1089–1098
12. G. Witucki, A Silane Primer: Chemistry and Applications of Alkoxy Silanes, *J. Coat. Technol.*, 1993, **65**(822), p 57–60
13. E. Metwalli, D. Haines, O. Becker, S. Conzone, and C.G. Pantano, Surface Characterizations of Mono-, Di-, and Tri-Aminosilane Treated Glass Substrates, *J. Colloid Interface Sci.*, 2006, **298**(2), p 825–831

14. R.A. Difelice, "An Investigation of Plasma Pretreatments and Plasma Polymerized Thin Films for Titanium/Polyimide Adhesion" (2001)

15. X. Yuan, Z.F. Yue, X. Chen, S.F. Wen, L. Li, and T. Feng, EIS Study of Effective Capacitance and Water Uptake Behaviors of Silicone-Epoxy Hybrid Coatings on Mild Steel, *Prog. Org. Coat.*, 2015, **86**, p 41–48

16. R. Figueira, I. Fontinha, C. Silva, and E. Pereira, Hybrid Sol-Gel Coatings: Smart and Green Materials for Corrosion Mitigation, *Coatings*, 2016, **6**(1), p 12

17. J. Wojciechowski, K. Szubert, R. Peipmann, M. Fritz, U. Schmidt, A. Bund, and G. Lota, Anti-Corrosive Properties of Silane Coatings Deposited on Anodised Aluminium, *Electrochim. Acta*, 2016, **220**, p 1–10

18. G.S. An, S.W. Choi, T.G. Kim, J.R. Shin, Y.I. Kim, S.C. Choi, and Y.G. Jung, Amino-Functionalization of Colloidal Alumina Particles for Enhancement of the Infiltration Behavior in a Silica-Based Ceramic Core, *Ceram. Int.*, 2017, **43**(1), p 157–161

19. Y.S. Lee, D. won Choi, B. Shong, S. Oh, and J.S. Park, Low Temperature Atomic Layer Deposition of SiO₂ thin Films Using Di-Isopropylaminosilane and Ozone, *Ceram. Int.*, 2017, **43**(2), p 2095–2099

20. L. Huang, Q. Jin, X. Qu, J. Jin, C. Jiang, W. Yang, L. Wang, and W. Shi, Characterization and Simulation on Antireflective Coating of Amorphous Silicon Oxide Thin Films with Gradient Refractive Index, *Superlattices Microstruct.*, 2016, **96**, p 198–204

21. J. Spivack, O. Siclovan, S. Gasaway, E. Williams, A. Yakimov, and J. Gui, Improved Efficiency of Dye Sensitized Solar Cells by Treatment of the Dyed Titania Electrode with Alkyl(Trialkoxy)Silanes, *Sol. Energy Mater. Sol. Cells*, 2006, **90**(9), p 1296–1307

22. N.P. Dasgupta, S. Xu, H.J. Jung, A. Iancu, R. Fasching, R. Sinclair, and F.B. Prinz, Nickel Silicide Nanowire Arrays for Anti-Reflective Electrodes in Photovoltaics, *Adv. Funct. Mater.*, 2012, **22**(17), p 3650–3657

23. J.L. Kepler and C.E. Locke, Evaluation of Corrosion Protection Methods for Reinforced Concrete Highway Structures, *Corrosion*, 2000, (58), p 231

24. K. Awsiuk, A. Budkowski, A. Psarouli, P. Petrou, A. Bernasik, S. Kakabakos, J. Rysz, and I. Raptis, Protein Adsorption and Covalent Bonding to Silicon Nitride Surfaces Modified with Organo-Silanes: Comparison Using AFM, Angle-Resolved XPS and Multivariate ToF-SIMS Analysis, *Colloids Surfaces B Biointerfaces*, 2013, **110**, p 217–224

25. M.P. Neupane, S.J. Lee, J.Y. Kang, I.S. Park, T.S. Bae, and M.H. Lee, Surface Characterization and Corrosion Behavior of Silanized Magnesium Coated with Graphene for Biomedical Application, *Mater. Chem. Phys*, 2015, **163**, p 229–235

26. L. Chen, Y. Wang, P. Fei, W. Jin, H. Xiong, and Z. Wang, Enhancing the Performance of Starch-Based Wood Adhesive by Silane Coupling Agent(KH570), *Int. J. Biol. Macromol.*, 2017, **104**, p 137–144

27. N. Wang, D. Xiong, M. Li, Y. Deng, Y. Shi, and K. Wang, Superhydrophobic Surface on Steel Substrate and Its Anti-Icing Property in Condensing Conditions, *Appl. Surf. Sci.*, 2015, **355**, p 226–232

28. F. de Buyl, Organo-Functional Silanes, in *Inorganic Polymers*, Nova Science Publishers Inc., Seneffe, Belgium, 2007, p 88–93

29. W.J. van Ooij, D. Zhu, V. Palanivel, J.A. Lamar, and M. Stacy, Overview: the Potential of Silanes for Chromate Replacement in Metal Finishing Industries, *Silicon Chem.*, 2006, **3**(1–2), p 11–30

30. U. Schubert, Chemistry and Fundamentals of the Sol-Gel Process, in *The Sol-Gel Handbook*, Wiley, Blackwell, 2015, p 1–28

31. Y. Liu, H. Cao, Y. Yu, and S. Chen, Corrosion Protection of Silane Coatings Modified by Carbon Nanotubes on Stainless Steel, *Int. J. Electrochem. Sci.*, 2015, **10**(4), p 3497–3509

32. L. Calabrese, V. Brancato, L. Bonaccorsi, A. Frazzica, A. Caprì, A. Freni, and E. Proverbio, Development and Characterization of Silane-Zeolite Adsorbent Coatings for Adsorption Heat Pump Applications, *Appl. Therm. Eng.*, 2017, **116**, p 364–371

33. K.J. Jothi and K. Palanivelu, Anti-Corrosion Coatings on SS 304 by Incorporation of Pr₆O₁₁–TiO₂ in Siloxane Network, *Surf. Eng. Appl. Electrochem*, 2015, **51**(6), p 589–597

34. P. Balan, M.J. Shelton, D.O.L. Ching, G.C. Han, and L.K. Palniandy, Modified Silane Films for Corrosion Protection of Mild Steel, *Procedia Mater. Sci.*, 2014, **6**(Icmpc), p 244–248

35. M. Longhi, S.R. Kunsta, L.V.R. Beltrami, E.K. Kerstner, C.I. Silva Filho, V.H.V. Sarmento, and C. Malfatti, Effect of Tetraethoxy-Silane (TEOS) Amounts on the Corrosion Prevention Properties of Siloxane-PMMA Hybrid Coatings on Galvanized Steel Substrates, *Mater. Res*, 2015, **18**(6), p 1140–1155

36. Z. Li, R. Wang, R.J. Young, L. Deng, F. Yang, L. Hao, W. Jiao, and W. Liu, Control of the Functionality of Graphene Oxide for Its Application in Epoxy Nanocomposites, *Polym. (U. K.)*, 2013, **54**(23), p 6437–6446

37. Y.J. Wan, L.X. Gong, L.C. Tang, L. Bin Wu, and J.X. Jiang, Mechanical Properties of Epoxy Composites Filled with Silane-Functionalized Graphene Oxide, *Compos. Part A Appl. Sci. Manuf.*, 2014, **64**, p 79–89

38. J. Yang, J. Xiao, J. Zeng, L. Bian, C. Peng, and F. Yang, Matrix Modification with Silane Coupling Agent for Carbon Fiber Reinforced Epoxy Composites, *Fibers Polym.*, 2013, **14**(5), p 759–766

39. A.J. Allen, J. Ilavsky, G.G. Long, J.S. Wallace, C.C. Berndt, and H. Herman, Microstructural Characterization of Yttria-Stabilized Zirconia Plasma-Sprayed Deposits Using Multiple Small-Angle Neutron Scattering, *Acta Mater.*, 2001, **49**(9), p 1661–1675

40. T. Gnaeupel-Herold, H.J. Prask, J. Barker, F.S. Biancaniello, R.D. Jiggetts, and J. Matejicek, Microstructure, Mechanical Properties, and Adhesion in IN625 Air Plasma Sprayed Coatings, *Mater. Sci. Eng. A*, 2006, **421**(1–2), p 77–85

41. F.J. Antunes, V.R.D.S. de Sá Brito, I.N. Bastos, and H.R.M. Costa, Characterization of FeCr and FeCoCr Alloy Coatings of Carbon Steels for Marine Environment Applications, *Appl. Adhes. Sci.*, 2013, **1**(1), p 1–10

42. R. Weber and O. De, "Method of Producing Chlorosilane," (United State of america, 2005)

43. P.V. Mehta and A.I. Ranka, Ionic Organosilicon Compounds and Compositions Thereof (India), United States Patent, 2009, p 11

44. ASTM G3-89, Standard Method for Conventions Applicable to Electrochemical Measurements in Corrosion Testing. in *Annual book of ASTM standards, Vol 03.02.*, (Conshohocken, PA, 2006)

45. M. Boutamine, A. Bellel, S. Sahli, Y. Segui, and P. Raynaud, Hexamethyldisiloxane Thin Films as Sensitive Coating for Quartz Crystal Microbalance Based Volatile Organic Compounds Sensors, *Thin Solid Films*, 2014, **552**, p 196–203

46. W.R. Ashurst, C. Yau, C. Carraro, R. Maboudian, and M.T. Dugger, Dichlorodimethylsilane as an Anti-Stiction Monolayer for MEMS: a Comparison to the Octadecyltrichlosilane Self-Assembled Monolayer, *J. Microelectromech. Syst.*, 2001, **10**(1), p 41–49

47. Q. Tao, H. He, T. Li, R.L. Frost, D. Zhang, and Z. He, Tailoring Surface Properties and Structure of Layered Double Hydroxides Using Silanes with Different Number of Functional Groups, *J. Solid State Chem*, 2014, **213**, p 176–181

48. A. Aydınoğlu and A.B.H. Yoruç, Effects of Silane-Modified Fillers on Properties of Dental Composite Resin, *Mater. Sci. Eng. C*, 2017, **79**, p 382–389

49. N. Soltani, N. Tavakkoli, M. Khayatkashani, M.R. Jalali, and A. Mosavizade, Green Approach to Corrosion Inhibition of 304 Stainless Steel in Hydrochloric Acid Solution by the Extract of Salvia Officinalis Leaves, *Corros. Sci.*, 2012, **62**, p 122–135

50. T.P. Chou, C. Chandrasekaran, S. Limmer, C. Nguyen, and G.Z. Cao, Organic-Inorganic Sol-Gel Coating for Corrosion Protection of Stainless Steel, *J. Mater. Sci. Lett.*, 2002, **21**(3), p 251–255

51. H. Cheraghi, M. Shahmiri, and Z. Sadeghian, Corrosion Behavior of TiO₂-NiO Nanocomposite Thin Films on AISI, 316L Stainless Steel Prepared by Sol-Gel Method, *Thin Solid Films*, 2012, **522**, p 289–296

52. J.R. Macdonald, J. Schoonman, and A.P. Lehnen, Applicability and Power of Complex Nonlinear Least Squares for the Analysis of Impedance and Admittance Data, *J. Electroanal. Chem. Interfacial Electrochem.*, 1982, **131**(C), p 77–95

53. G.W. Walter, A Review of Impedance Plot Methods Used for Corrosion Performance Analysis of Painted Metals, *Corros. Sci.*, 1986, **26**(9), p 681–703

54. H. Cesiulis, N. Tsyntsaru, A. Ramanavicius, and G. Ragoisha, *Nanostructures and Thin Films for Multifunctional Applications*, Springer, Berlin, 2016, p 3–43